
Article:
Carruthers, A.W., Shahmir, H., Rigby, M. orcid.org/0000-0002-3421-2541 et al. (2 more authors) (2023) Using concentration gradients to examine the effects of Al, Ga and Sn additions on the low-activation VCrMnFe system. Journal of Physics: Energy, 5 (2). 024013. ISSN 2515-7655

https://doi.org/10.1088/2515-7655/acc3c1

JPhys Energy

PAPER • OPEN ACCESS

Using concentration gradients to examine the effects of Al, Ga and Sn additions on the low-activation VCrMnFe system

To cite this article: A W Carruthers *et al* 2023 *J. Phys. Energy* **5** 024013

Journal of Physics: Energy

PAPER

Using concentration gradients to examine the effects of Al, Ga and Sn additions on the low-activation VCrMnFe system

A W Carruthers[1,*], H Shahmir[2], M Rigby[1], A S Gandy[2] and E J Pickering[1,3]

[1] Department of Materials, University of Manchester, Manchester M13 9PL, United Kingdom
[2] Department of Materials Science and Engineering, University of Sheffield, Sheffield S1 3JD, United Kingdom
[3] Henry Royce Institute for Advanced Materials, Manchester M13 9PL, United Kingdom
[*] Author to whom any correspondence should be addressed.

E-mail: alexander.carruthers@manchester.ac.uk

Keywords: low-activation alloys, high-entropy alloys, multi-principal element alloys, alloys for fusion, VCrMnFe, VCrMnFeAl$_x$

OPEN ACCESS

RECEIVED
30 September 2022

REVISED
16 February 2023

ACCEPTED FOR PUBLICATION
13 March 2023

PUBLISHED
3 April 2023

Abstract

A critical design criterion for future fusion reactor components is low activation. The equiatomic multi-principal element alloy VCrMnFe is comprised solely of low activation elements and forms a single-phase solid solution at temperatures over 1000 °C. However, at lower temperatures it forms detrimental sigma phase. In this work, compositional gradients of Ga, Sn or Al were induced in VCrMnFe using only a furnace to investigate their effect on intermetallic formation. By examining how the microstructure changed across a region with varying composition, phase stability limits could be assessed. For example, all three elements were found to prevent sigma phase from forming within the alloy when they were present at relatively low concentrations (2–5 at%). Al was found to be the most promising addition (in terms of not causing embrittlement), and the approach used enabled the characterisation of the VCrMnFe–Al pseudo binary phase diagram up to 50 at% Al after heat treatment of 800 °C/240 h followed by ageing at 600 °C/240 h, with numerous ordered phases found using electron diffraction. The level of Al addition required to suppress the sigma phase has been identified more precisely, which will be useful for future alloy development work.

1. Introduction

Some alloys based on multiple principal alloying elements (including so-called 'high-entropy alloys' and 'multi-principal element alloys') have been reported to display promising high temperature phase stability as well as resistance to radiation damage [1, 2]. Hence, they are now being explored for use in future fusion reactors as structural and plasma facing materials. A critical design requirement for materials to be used in commercial fusion power stations is that they are 'low activation', such that fusion neutrons do not induce high levels of radioactivity following service. Indeed, a common target is to use materials that should be deposable as low-level waste approximately 100 years following their removal from a fusion device. With this in mind, over recent years a number of studies have examined the development of multi-principal element alloys based on low-activation elements [3–6].

One of the reasons multi-principal element alloys have attracted so much interest in recent years is the vast compositional space that has been opened by their discovery. However, this also presents a key challenge—there are countless combinations of elements to study, even when only low-activation ones are considered. This had led to the development of methods for the rapid production of alloys with varied, but controlled, compositions [7–14]. The majority of these methods require expensive and/or custom-built equipment, e.g. powder additive manufacturing [10]. However, a simpler approach that may be used is the use of a diffusion couple to form the desired concentration gradients [14]. In its most basic form, a diffusion couple consists of two dissimilar blocks of material that are held together at high temperature, leading to the inter-diffusion of elements and the formation of gradients of composition across the materials. In this work, we investigate the use of a such an approach to examine the phase structure of alloys formed by additions of a fifth element to the equiatomic low-activation quaternary alloy VCrMnFe.

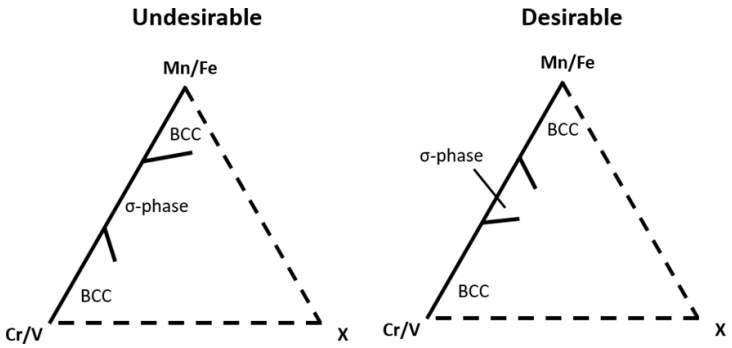

Figure 1. Schematic of the search criteria for an alloying element to prevent sigma phase formation in VCrMnFe using ternary phase diagrams.

VCrMnFe is a low-activation multi-principal element alloy, which is stable as a single body-centred cubic (BCC) phase above 1000 °C. Unfortunately, at temperatures below 1000 °C, it forms a sigma phase, which is undesirable owing to its brittle nature [15–18]. Small additions of Al have been shown to stop the sigma-phase from forming [18]. However, only discrete concentrations of Al have been investigated to date (2.3, 6.6, 10.5 and 21 at%, with sigma phase being repelled between 2.3 and 6.6 at%), and hence it has not been possible to pinpoint the composition at which sigma phase is destabilised. Furthermore, it has been found that these discrete additions of Al to VCrMnFe result in the formation of multiple ordered phases, particularly at higher Al contents. Hence, this paper has the primary objective to investigate the effects of Al additions to VCrMnFe more thoroughly by examining a continuous range of Al concentrations via a diffusion couple.

A secondary objective of this work was to rapidly examine the effects of additions of other alloying elements on the VCrMnFe system. Elemental additions other than Al are of interest because small Al additions, which were insufficient to inhibit all of the sigma phase from forming, were found to cause ordering in the matrix of the $VCrMnFeAl_{0.1}$ alloy [18]. It may be that this ordering is found to be undesirable, and hence other elements that stop the formation of sigma-phase without inducing ordering are of interest. Using the principle outlined in [18] and reproduced in figure 1, low-activation elements were sought that would shrink the sigma phase field (i.e. destabilise sigma). Ga [19] and Sn [20] were identified as promising candidates for this in the VCrMnFe system. 'Low-activation' here is defined as the time taken to decay to 'low level waste' after ∼5 years of pulsed operation in the DEMO nuclear reactor divertor body [3, 4].

In this work, equi-atomic VCrMnFe was exposed to high temperatures with small amounts of each of the three elements (Al, Ga and Sn) placed on top. Owing to the low melting point of the elements, they diffused rapidly into the VCrMnFe alloy and created a concentration gradient across the surface of the sample on the order of microns, which enabled analysis using scanning and transmission electron microscopy (SEM and TEM). Here, we report on the phases formed in alloys and discuss whether the addition of these elements produces alloy compositions that could be candidates for future fusion materials.

Thus, this heat treatment was designed to allow for diffusion into the alloy, as well as maximise the ability of the alloy to form sigma-phase, both with regards to kinetics and stability.

2. Experimental

A VCrMnFe billet was produced by vacuum arc melting, using an Arcast 200 arc melter in an Ar atmosphere, with elemental metals of purity >99.8% (Goodfellow Cambridge Ltd, Cambridge, UK). The billet produced was flipped and remelted at least five times to facilitate homogonous mixing of the elements. The alloy composition was determined by energy dispersive x-ray analysis (EDX) in an SEM and was reported previously in [18] and given here in table 1. The as-cast billet was then homogenised at 1200 °C for 100 h, under flowing Ar, and quenched in water. This procedure has been previously reported to result in the formation of a BCC single phase solid solution [15, 18]. The billet was sectioned into 3 pieces, and a piece (around 25 g) of high purity (>99.9%) Ga, Sn and Al was placed on top of each piece. A heat treatment was used to facilitate diffusion of the elemental metals into the VCrMnFe alloy. The elemental additions (Ga, Sn, Al) used in this study all have a low melting temperature (30, 232 and 660 °C respectively). It was possible therefore to use an aging temperature greater than the melting temperature of the three alloying additions, increasing the contact area between the elements and the alloys, improving diffusivity between them. It has previously been reported that, at the contact, the VCrMnFe could also be partially melted, increasing the

Table 1. Alloy compositions as calculated by SEM-EDX (at%).

V	Cr	Mn	Fe
26.1 ± 0.2	25.6 ± 0.3	24.7 ± 0.3	23.6 ± 0.3

contact and diffusivity between the two layers, reducing the need for a clamping force being applied during heating [14]. Based on the melting temperatures of the elements, the pieces were aged at 800 °C for 240 h in an Ar atmosphere, then furnace cooled. Following this, the diffusion couples were further aged at 600 °C for 240 h and water quenched, since intermetallic phases such as sigma tend to be more thermodynamically stable at lower temperatures. Thus, the heat treatment schedule used was designed to allow for diffusion into the alloy (at 800 °C), as well as maximising the opportunity for sigma phase formation (at 600 °C).

Elemental distributions, microstructures and crystal structures across the diffusion bond (element-alloy interface) were determined by SEM/EDX and electron backscatter diffraction (EBSD), using a Zeiss Merlin with Oxford Instruments EDX and EBSD detectors. Low voltage EDX data was collected using an Oxford Xmax extreme detector. Samples were mechanically polished to a final stage that used 0.05 μm colloidal silica as the polishing medium. EDX and EBSD maps were collected using a beam energy of 20 keV, unless otherwise stated. All SEM-EDX maps were quantified in terms of at% using Oxford Instruments' Aztec 4.0 software.

Whilst EBSD can determine many different phases (crystal structures) in an alloy, it is not able to detect the difference between BCC (A2), and ordered superlattice structures based on BCC, e.g. B2. Therefore, electron diffraction analysis was undertaken for the alloy comprising extra Al additions to determine the exact phase structures present. Electron transparent lamellae were prepared for TEM analysis using the focused Ga^+ ion beam *in-situ* lift-out method [21] with an FEI Helios 660 NanoLab FIB-SEM. The Ga^+ beam was operated at 1 kV, 5 kV and 30 kV, with a beam current of 12 Pa–9 nA. The lamellae were analysed using a 200 keV, X-FEG FEI Talos F200 S/TEM. S/TEM-EDX data were quantified and are presented in at%. The Cliff–Lorimer methodwas used for quantification, using a thickness of 70 nm for absorption correction.

3. Results and discussion

3.1. Ga addition

Figure 2 shows SEM results of the VCrMnFe with Ga addition, including compositional information obtained using EDX and phase and crystallographic information obtained using EBSD. The pure Ga was placed on the top of the sample above the region shown in figure 2(a) (as indicated by the text at the top of figure 2(a)), and the region shown in the figure corresponds to the area where sigma phase was first seen to form moving away from the surface. Of the three elemental additions, Ga had shallowest concentration gradient through the depth of the sample, making the sigma phase limiting concentration easiest to identify.

The Ga concentration can be seen to be highest nearest the top surface of the alloy, as expected. However, the gradient is not perfectly vertical from top to bottom. The EDX data indicates the Ga diffused over 1 mm into the alloy. Given the length scale over which the diffusion occurred, it is likely that during heating some Ga spilled over the side and diffused in from multiple directions, creating a slightly more complex compositional profile. However, the directionality of the concentration profile is not particularly important to this study as the goal was to produce a range of compositions throughout the alloy and specific phase compositions can be determined by EDX.

The EBSD phase map in figure 2(a) indicates an entirely BCC microstructure nearer the Ga-richer top of the sample, with the sigma phase visible in the phase map at the bottom, shown as very small green regions in the map. Figure 2(b) shows a higher magnification image around the region where sigma phase is first observed. The EDX line scan in figure 2(c) shows the Ga composition at the region where sigma phase first forms in the matrix. The matrix, rather than the grain boundaries, was examined via SEM as Ga enrichment can be seen at the grain boundaries, the implications of this are discussed later. From this, the Ga concentration necessary to prevent sigma phase from forming was found to be 3.0 ± 0.5 at%.

That Ga is supressing the formation of sigma phase is further corroborated by the fact that it is reduced in concentration in the sigma phase, relative to the surrounding matrix. The Ga concentration in the sigma-phase in the highest Ga content regions where it formed was measured as 0.5 ± 0.2 at%. Unfortunately, the Ga addition was seen to embrittle the grain boundaries to the point where no boundaries in the sample were observed not to contain cracks.

Figure 3 shows results from closer to the top of the sample, above figure 2 (i.e. more Ga-enriched), from a region that had a Ga concentration of 27.0 ± 0.7 at%. The presence of a fine 2nd phase, in significant quantities, is noted. This phase was indexed as M_3Ga, where M = V, Cr (with a Cr_3Si-like structure). This

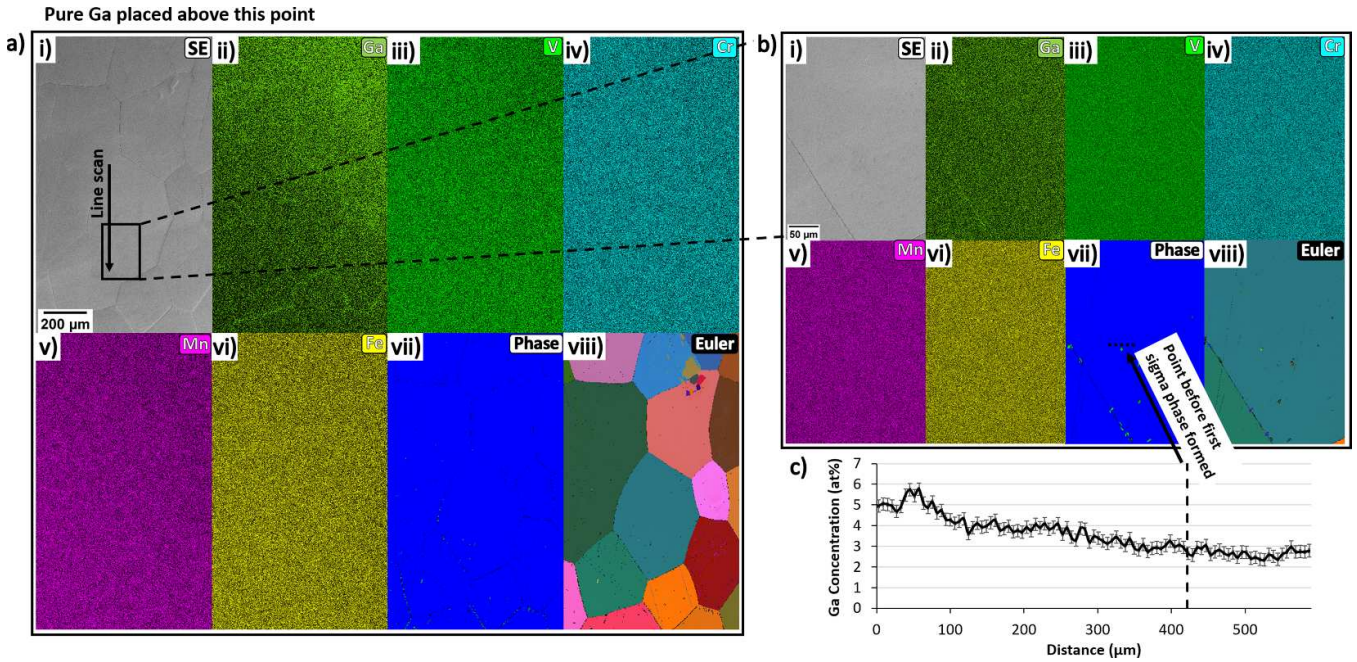

Figure 2. SEM micrographs of VCrMnFe + Ga taken from below the top surface of the sample. (a) Overview of the Ga segregation through the alloy (the pure Ga was placed above the top of the figure, as noted), (b) higher magnification image from the Ga poor region. (i) SE images, (ii)–(vi) SEM-EDX maps. (vii) and (viii) show the EBSD phase and Euler angle maps of the regions respectively. (c) Shows the EDX line-profile from the line highlighted in (a) (i) of the Ga enrichment with the edge of the first sigma phase shown. In the phase maps blue = bcc and green = sigma.

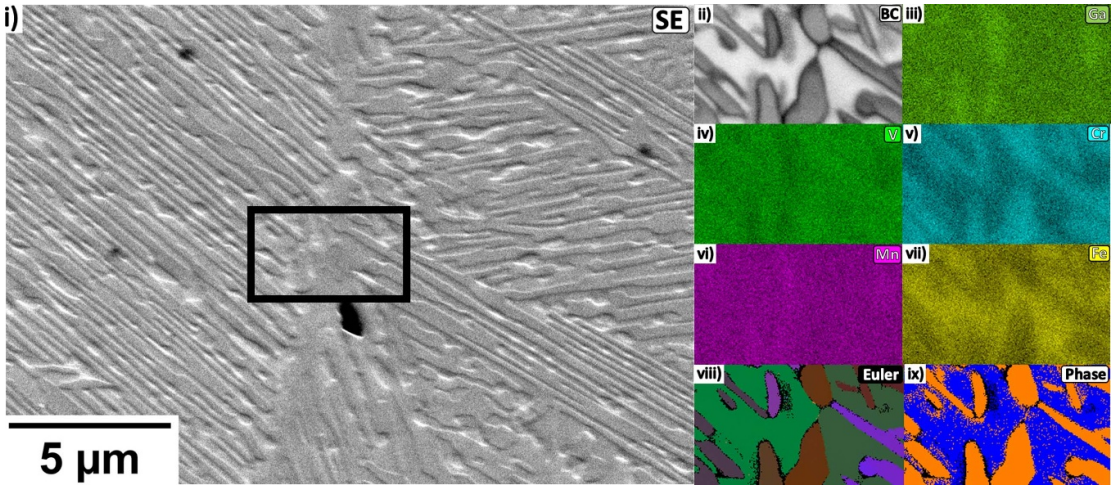

Figure 3. SEM analysis of VCrMnFe + Ga, above figure 2, where Ga = 27 at%. (i) SE image, (ii) Band contrast, (iii)–(vii) EDX spectrum maps and EBSD (viii) Euler angle map and (ix) phase map. In the phase map blue = BCC and orange = M_3Ga.

microstructure formed a second region at the top of the sample that was distinct from that in below it (shown in figure 2).

3.2. Sn addition

The microstructure of the Sn-enriched regions shown in figure 4 is more complex than the sample with Ga additions. The Sn-enriched region is located in the top half of each image shown in figures 4(a) and (b). Figures 4(b) (i)–(viii) are magnified SEM/EDX data taken from the region indicated by the box in figure 4(a) (i). Within figure 4(b) (viii), several regions can be seen (labelled (A)–(E) in figure 4(b) (viii)). There are two regions indexed as BCC with varying Sn and Mn enrichment (A and B), a tertiary Sn rich phase (C), and sigma phase (D). The average composition of the Sn-enriched region is also given in (E). Their concentrations are shown in table 2. The Euler angle maps presented (which show distinct crystallographic orientations) in figure 4 and later in this work are presented simply to highlight distinct grains.

Region C can be seen to be a separate phase and was indexed as the hexagonal phase, M_3Sn, where M = Mn, Fe, V [22, 23]. Sn is present at ∼25 at% in this phase and V, Fe and Mn are also present in substantial quantities, which is consistent with the expected composition of M_3Sn. Further to this, Cr_3Sn was not found in a search of the literature as a previously reported phase (with the same structure as that of $(V,Mn,Fe)_3Sn$). This suggests that Cr_3Sn is less likely to be a stable phase, which corroborates the observed lower quantities of Cr in the M_3Sn phase.

There is no evidence of the sigma-phase in regions of the alloy at higher Sn concentrations, shown at the top of figure 4(b). It is suggested, therefore, that in these regions, B and E, sigma phase formation was supressed. Figure 4(c) gives the concentration of elements in at% across the red line denoted in figure 4(b) (viii), with the vertical dashed line in figure 4(c) indicating the point at which the sigma-phase is first observed to form. The data presented in figure 4(c) and in table 2 indicate that 2 ± 0.8 at% Sn and 2.6 ± 0.1 at% Sn (region B) respectively is necessary to prevent sigma phase from forming in the alloy system. The discrepancy arises from the composition being calculated as an average across this region in table 2, whereas there is a slight compositional variation across it, which is captured in the EDX line scan in figure 4(c).

However, in this boundary region, the M_3Sn phase was also still present. Indeed, there is an M_3Sn particle adjacent to the particle of sigma phase highlighted by an arrow in figure 4(b). Note also that this particle appears to be within the matrix of the alloy, and not on a grain boundary. Thus, whilst sufficient quantities of Sn may prevent sigma formation in this alloy system, it will stabilise a third, hexagonal, M_3Sn phase, before doing so. This conclusion is made more complex, however, by the clear reduction of Mn in the Sn-enriched region. This has fundamentally changed the composition of the base VCrMnFe alloy, and is considered further in the discussion.

3.3. Al addition

Figure 5 shows an SEM image of the Al-enriched layers induced within the VCrMnFe alloy (the top of the image is the surface on which the pure Al was placed). An EDX line scan shows 3 distinct compositional regions with respect to Al content. Figure 6 shows a higher magnification image across the boundary

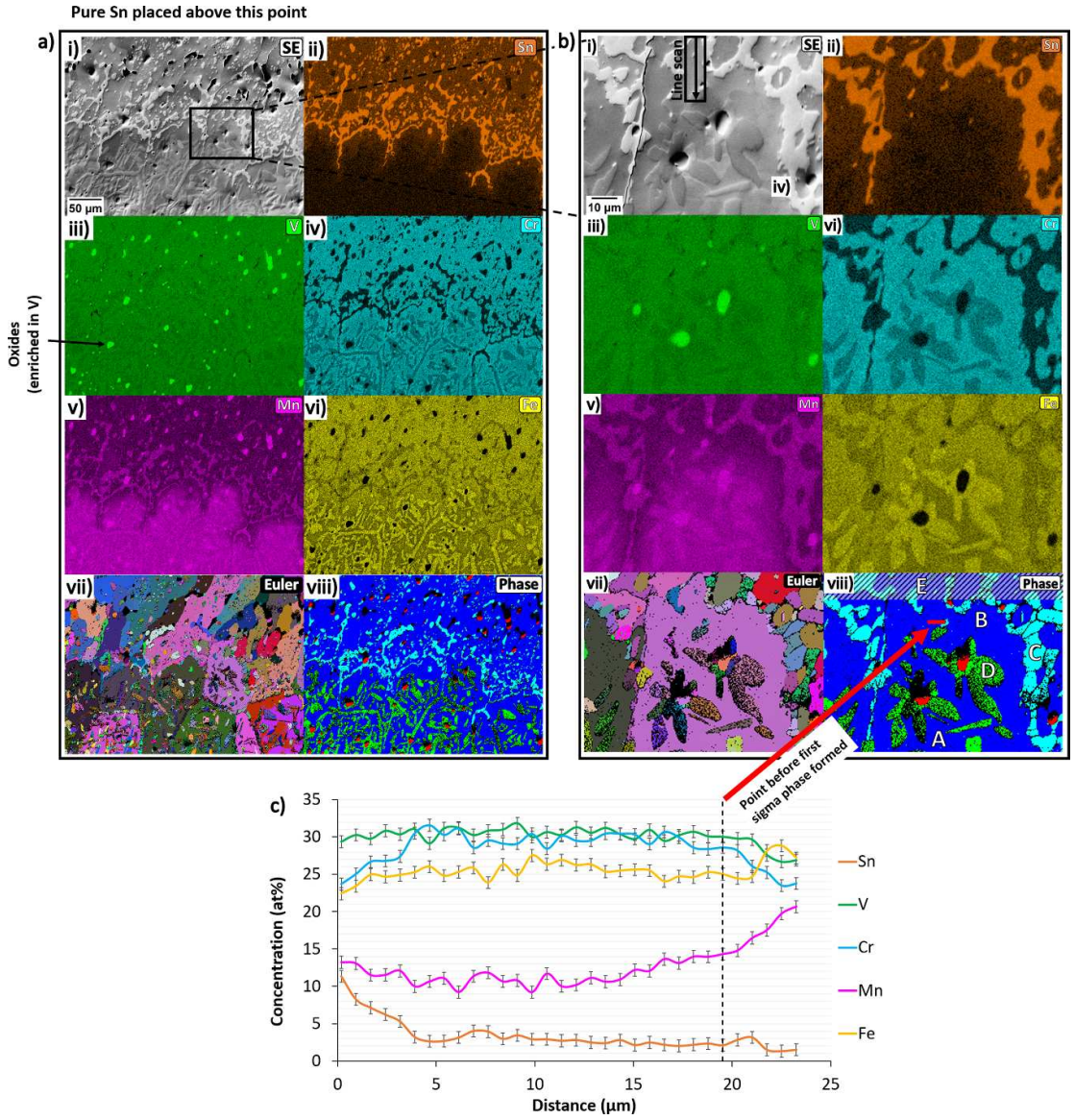

Figure 4. (a) Overview of the Sn segregation through the alloy (the Sn placed above the top of the image), (b) higher magnification images from the Sn rich–Sn poor boundary. (i) SEM SE images of VCrMnFe + Sn. (ii)–(vi) SEM-EDX maps, EBSD (vii) Euler angle map and (viii) phase map. In the phase maps, blue = bcc, green = sigma, red = vanadium oxide and cyan = M_3Sn. Note vanadium oxides were found to be present in the material prior to aging with Sn. The five regions quantified in table 2 are highlighted in (b) (viii). (c) shows the result of the EDX line scan carried out across the area shown in (b) (i).

Table 2. Compositions of phases within VCrMnFe + Sn in at% as extracted from the SEM-EDX map shown in figure 4.

Label	Region	V	Cr	Mn	Fe	Sn
A	Sn poor BCC	28.6 ± 0.3	29.3 ± 0.3	20.5 ± 0.2	20.7 ± 0.2	0.9 ± 0.1
B	BCC (edge of Sn-enriched region)	30.3 ± 0.3	29.4 ± 0.3	12.6 ± 0.2	25.1 ± 0.2	2.6 ± 0.1
C	M_3Sn	26.4 ± 0.3	8.7 ± 0.2	19.6 ± 0.2	19.7 ± 0.2	25.7 ± 0.3
D	Sigma	25.8 ± 0.3	21.8 ± 0.3	23.9 ± 0.2	27.9 ± 0.3	0.66 ± 0.1
E	Sn rich average	31.3 ± 0.3	27.6 ± 0.3	11.4 ± 0.2	24.7 ± 0.3	5.1 ± 0.1

between the medium and low Al concentration regions. Sigma phase can be seen in the low Al concentration region, but its presence abruptly stops at the boundary. From the line scan presented in figure 5 (ii) Al was found to diffuse to approximately 260 μm from the diffusion couple interface. Compared to the diffusion distance of Ge and Sn, the diffusion of Al into the sample was relatively limited (as might be expected owing to its higher melting point). Three regions of Al concentration (hereafter referred to as high, medium and low), are shown in figure 5. The sigma phase was seen to stop forming at the boundary between the low and medium Al regions, see figure 6.

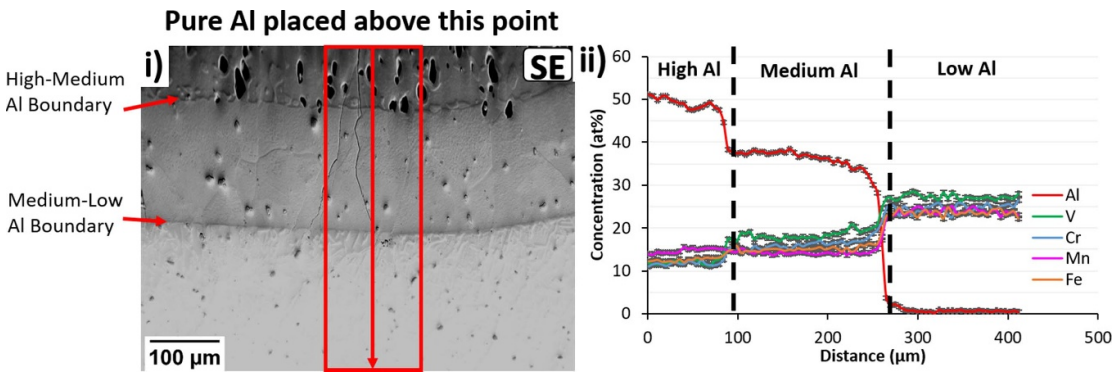

Figure 5. (i) SE image and (ii) EDX line-scan through a cross section of VCrMnFe + Al. Three distinct compositional regions can be seen. The zero distance in (ii) is the top of the mage in (i).

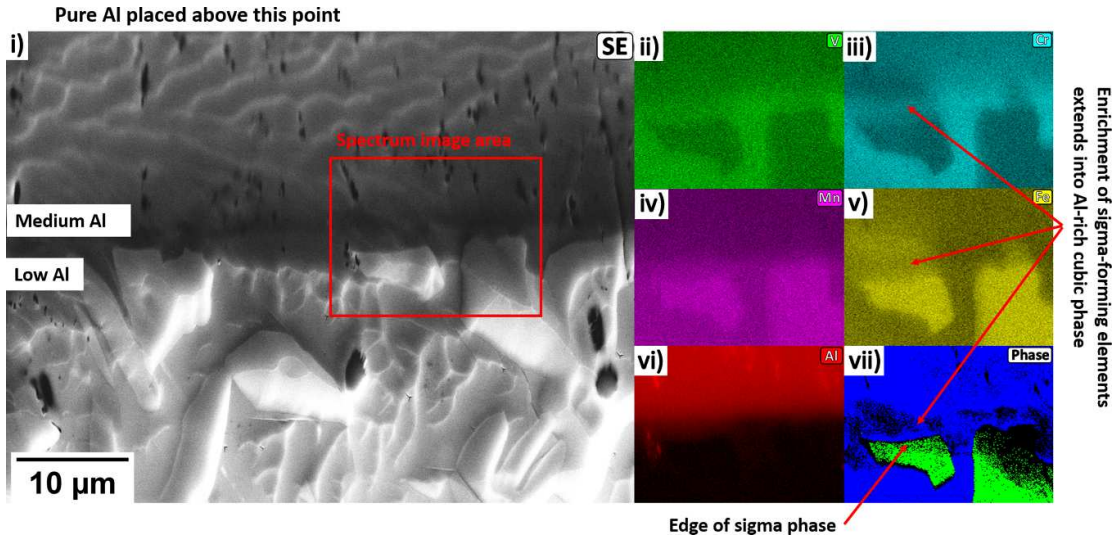

Figure 6. Boundary between the ∼30 at% Al (top) and ∼0 at% Al (bottom) regions of VCrMnFe + Al. (i) SE image, (ii)–(vi) EDX spectrum images and (vii) phase map (blue = bcc and green = sigma, black = unindexed).

The rapid change in Al concentration shown in figure 6 made quantifying the exact Al concentration at which the sigma phase stopped forming not possible with the data shown in figure 6. A lower beam current of 3 kV was used (along with the XMax-extreme detector) in order to reduce the beam interaction with the sample to a smaller volume, thereby improving the spatial resolution. Figure 7(a) shows an SEM image across the low-medium Al concentration boundary. From the EDX line-scan across the boundary between the BCC and sigma phases in figure 7(b), the Al concentration at the edge of the boundary is estimated as 4 ± 0.5 at% Al. The Al concentration measured in the sigma phase is similar to previously measured concentrations of Al in a VCrMnFe alloy containing 2.3 at% Al [18].

Figure 6 shows regions enriched in elements, with compositions similar to that of sigma phase, extending out of the sigma phases and into the region containing higher Al, whilst the EBSD phase data shows a BCC structure in these areas. This indicates that the sigma phase was present in this region, but dissolved with increasing Al content in the region. This demonstrates that confidence can be given that figure 7(b) shows the necessary Al content to prevent sigma phase formation, rather than simply the position that the sigma phase stops.

In order to investigate further the elemental distribution across the interfaces in the Al containing alloy, two FIB foils, one from across each boundary region depicted in figure 5 (i), were extracted. The use of FIB foils enabled the rapid change in Al concentration gradients to be captured in a single foil. TEM was then used to determine structures across the interfaces that are indiscernible from the BCC phase found in the EBSD [18].

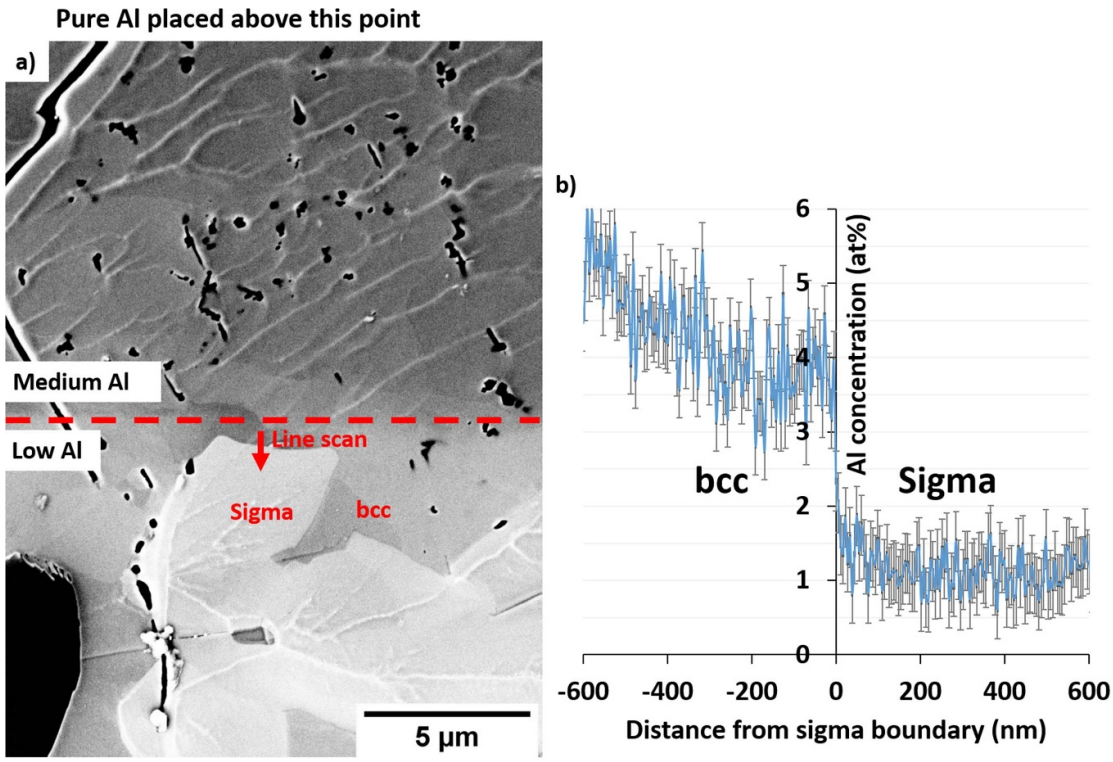

Figure 7. (a) SEM SE image of the boundary between the low and medium Al regions. (b) SEM-EDX line scan showing the Al content across the boundary into a region of sigma phase adjacent to the low-medium Al boundary (red arrow).

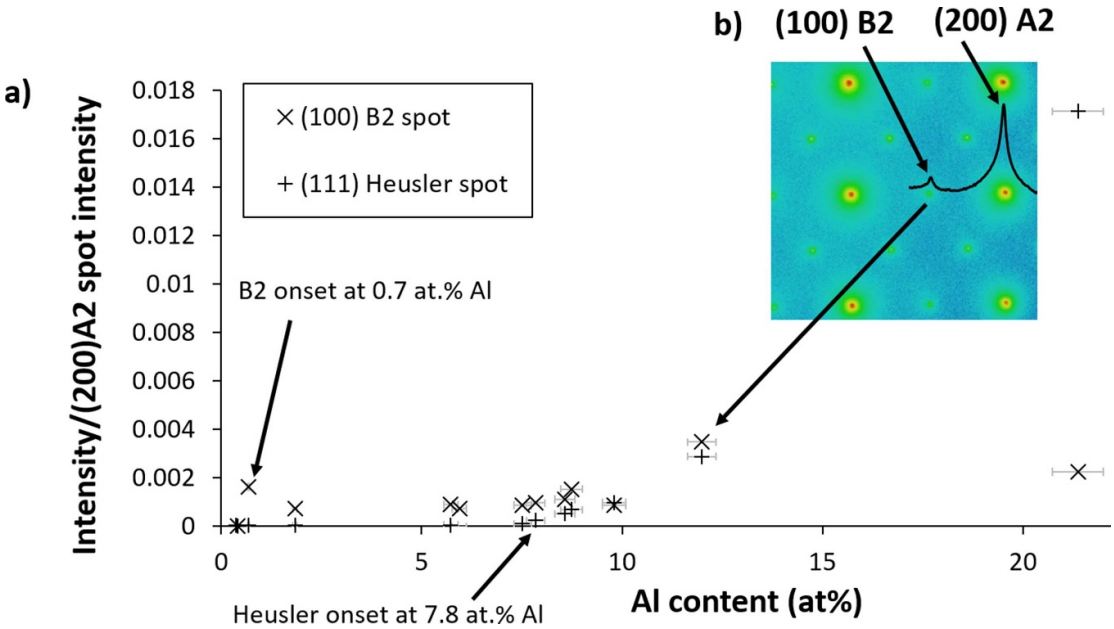

Figure 8. (a) Intensity of reflections of (100) B2 and (111) Heusler reflections relative to the (200) A2 reflection as a function of Al content in $VCrMnFeAl_x$. (b) shows a representative diffraction pattern and intensity plot, the arrow denotes the specific data point that it pertains to.

3.3.1. Low–medium Al boundary (0–30 at%)

A series of selected area diffraction patterns (SADPs) were taken across the interface. After each SADP was taken with a parallel electron beam, the beam was converged and point EDX spectra taken from the region, the results of this are shown in figure 8. The beam was orientated parallel to the [110] direction in the specimen, with the exception of minor bending, the region had the same orientation across the border. This enabled the Al concentrations at which different phases were stable to be determined. Figure 8 shows the intensity of electron diffraction spots arising from BCC superlattice (specifically B2 and Heusler phases)

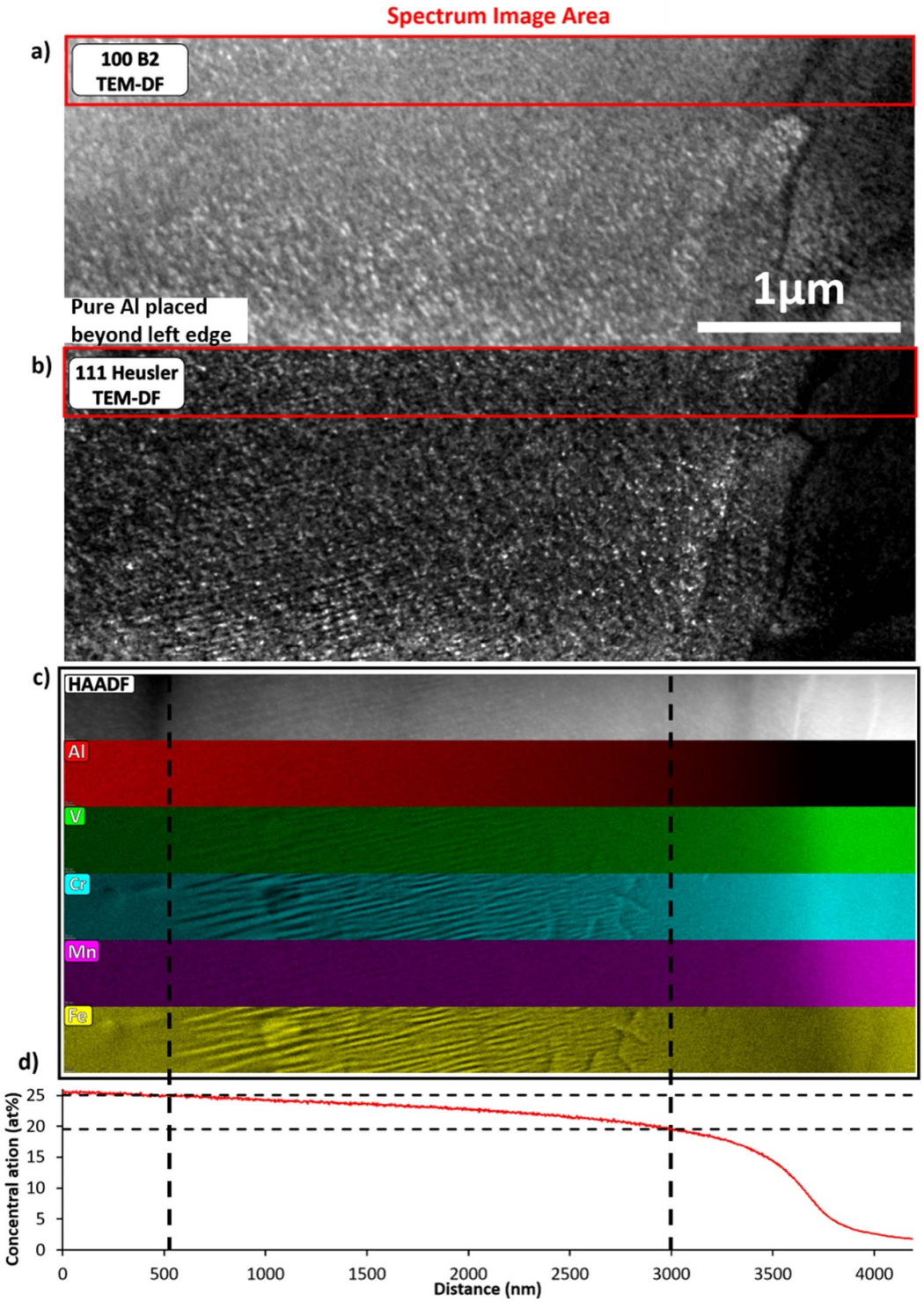

Figure 9. TEM-dark fields (DFs) across the medium–low Al boundary, using a B2 (100) type (a) and a Heusler (111) type (b) reflection. (c) STEM-HAADF and EDX elemental maps of the red region. (d) shows the quantified Al content across this region. The two phase region can be seen to occur between Al contents of 19.5–25 at%.

reflections within the alloy at different Al concentrations. The data presented in figure 8 suggest the B2 phase is stable at very low Al concentrations with the onset of (100) reflections at 0.7 at% Al. Very faint (111) type Heusler phase ($L2_1$ structure) reflections were visible at 7.8 at% Al. These results are fully consistent with previous work [18], which found (after aging at 600 °C) Heusler phase reflections in a $VCrMnFeAl_x$ alloy containing 10.8 at% Al, B2 reflections in the alloys containing 6.6 and 2.3 at% Al, and A2 reflections in an Al-free alloy.

Figure 9 shows a STEM-EDX map taken across the region of significant Al variation. Towards the left hand (Al richer) side of these images, stripes can be seen, in both the high-angle annular dark field

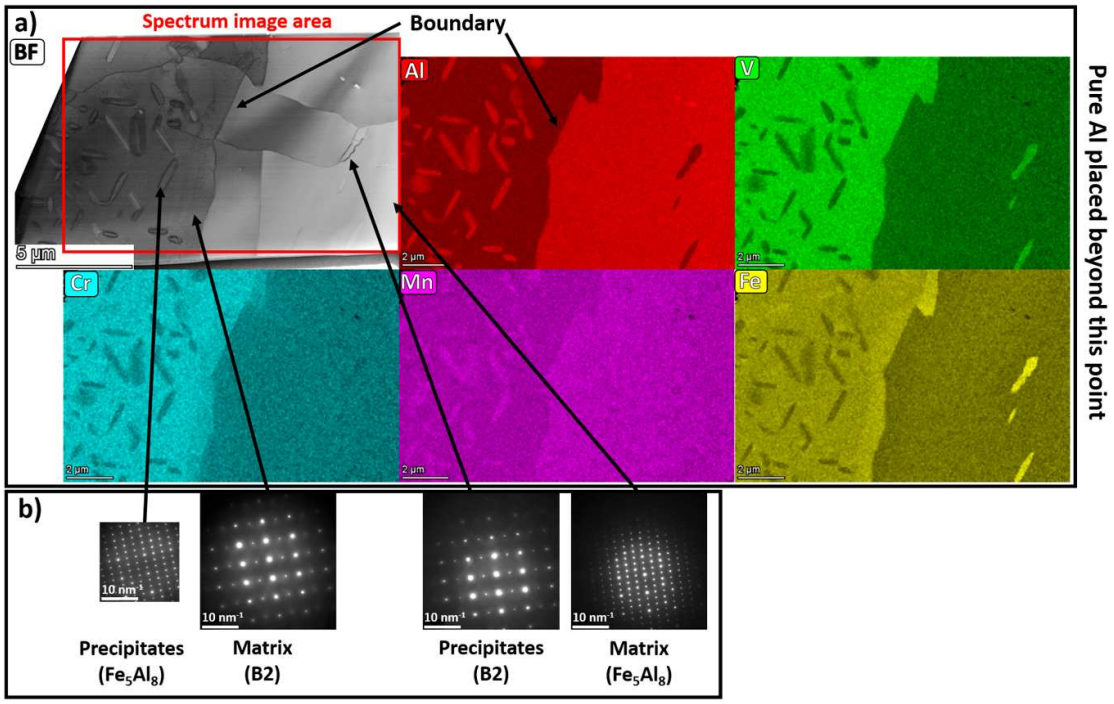

Figure 10. (a) STEM-bright field and EDX elemental maps of a FIB foil taken across the boundary of the medium–high Al regions. (b) SADPs down the [110] zone axis taken from the matrices and precipitates in both regions.

(HAADF), and the dark field (DF) image taken using the (111) Heusler type reflection. These stripes correspond to chemical segregation seen in the Fe and Cr elemental maps shown in figure 9(c), which are anti-correlated. The bright regions in figure 9(b) are ascribed to the Fe-enriched regions, which were created using the 111 type Heusler reflection. These are analogous to the structures seen in $VCrMnFeAl_{1.0}$ [18] which was aged at 800 °C.

Figure 9(d) shows that this striped region is only stable over a certain range of Al concentrations, specifically 19.5–25 at% Al. Furthermore, at concentrations >25 at% Al, the SADPs show only a B2 not a Heusler structure. At lower Al concentrations (the right hand side of figure 9), the DF images show a reduction in intensity of the bright regions, ascribed to the Heusler phase, with reducing Al content, until they completely disappear at around 7 at% Al, which is consistent with the data presented in figure 8(a).

The stripes in the two-phase region can be seen to be thicker at higher Al concentrations. This is likely a diffusion-related effect. The stripes at the higher Al concentrations would have spent more time at temperature in the two-phase region (with respect to Al content) as the Al diffused further into the material, meaning they had more time to coarsen.

3.3.2. Medium–high Al boundary (30–50 at%)

The border between the medium and high Al regions is shown in the bright field TEM image presented in figure 10(a). From the corresponding elemental maps, precipitates can be seen in both regions. SADPs from different regions of interest are shown in figure 9(b). As with the left edge of the specimen in figure 9 (lower Al), the matrix of the medium Al region was indexed to the B2 phase. The precipitates were indexed as Fe_5Al_8 (phase prototype: Cu_5Zn_8, space group 217). This is another cubic structure with a unit cell lattice parameter ∼3 times greater than the BCC/B2 phases seen in the material (8.8 and 2.9 Å respectively). In the high-Al region, the situation is reversed: the matrix was indexed as Fe_5Al_8, whilst the precipitates were indexed as B2. The diffraction patterns presented in figure 9(b) are all of the same orientation indicating that all phases in the TEM foil are coherent with each other.

The compositions, measured by STEM-EDX, of the phases identified in figure 10 are given in table 3. This data shows that the compositions of the B2 phases and Fe_5Al_8 phases measured in each region are similar. The exception being the Cr and Fe contents in the two B2 phases. The Fe and Cr contents are significantly higher and lower, respectively, in the B2 precipitates in the high-Al region compared with the B2 matrix of the medium-Al region. This is contrary to the results of figure 9 which shows Cr enriched and Fe depleted in the B2 phase in the two-phase region (19.5–25 at% Al). This suggests that the Fe_5Al_8 phase is more sensitive to Cr and Fe contents than the B2 phase. For instance, the Cr content of the Fe_5Al_8 precipitates is lower than

Table 3. Compositions of the phases observed in figure 10 as measured by STEM-EDX.

Region	Al	V	Cr	Mn	Fe
B2 matrix	31.1 ± 0.3	18.7 ± 0.2	17 ± 0.2	14.7 ± 0.1	18.5 ± 0.2
Fe_5Al_8 precipitates in B2 matrix	47.8 ± 0.8	11 ± 0.4	11.7 ± 0.3	16.8 ± 0.3	12.7 ± 0.3
Fe_5Al_8 matrix	49.6 ± 0.5	9.5 ± 0.1	10.9 ± 0.1	16 ± 0.2	14 ± 0.1
B2 precipitates in Fe_5Al_8 matrix	33.4 ± 0.3	15.2 ± 0.2	9.5 ± 0.2	14.9 ± 0.2	27 ± 0.3

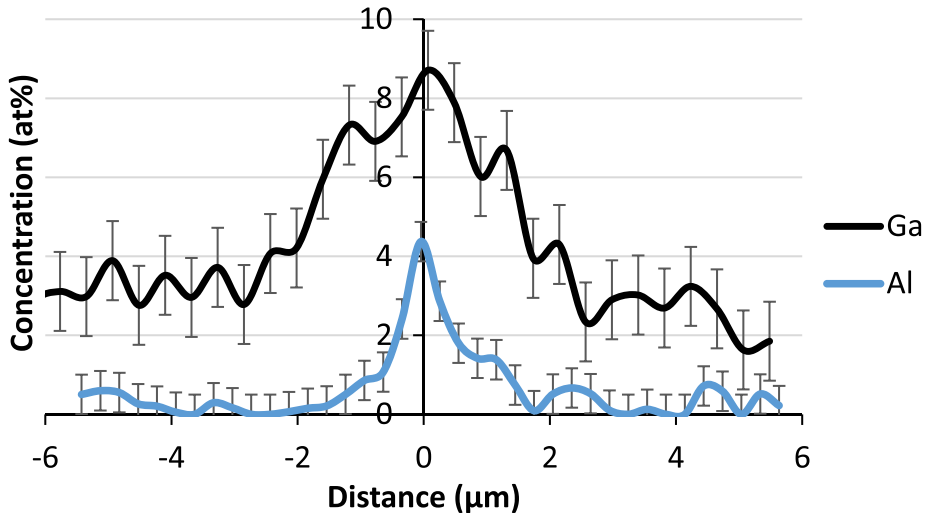

Figure 11. SEM-EDX line profiles across grain boundaries in regions of VCrMnFe + Ga and Al, near where sigma phase begins to form.

that of the surrounding B2 matrix, but the Fe_5Al_8 matrix has a similar Cr content to the B2 precipitates within it. This suggests a relatively narrow window of Cr contents are stable within the Fe_5Al_8 phase.

4. Further discussion

4.1. Grain boundary enrichment

Figures 2 and 4 indicate significant enrichment of Ga and Sn at grain boundaries. There are two possibilities for this, which are not necessarily mutually exclusive. The elements could have preferentially diffused along the grain boundaries, or preferentially occupied the grain boundaries, which would be seen in a homogenised material as well. These two mechanisms cannot be explicitly distinguished in this study. Even a homogenised material that showed Ga and Sn enrichment at the grain boundaries would not be definitive, as this would not preclude further preferential diffusion along them in the materials examined in this study. Ga and Sn are well known to segregate to grain boundaries (e.g. [24, 25]). However, it is also likely that there was preferential diffusion along the grain boundaries, as enrichment in Al was seen along boundaries (see figure 11), which was not observed in homogenised billets of VCrMnFe + Al [18].

4.1.1. Matrix vs. bulk compositions

Grain boundary segregation introduces errors when relating the observed concentrations of Ga, Sn and Al to their expected concentrations in the matrix of a homogenised alloy. In the case of Al, the matrix concentrations can be taken to be equal to their expected matrix concentrations in a homogenised alloy because, as already stated, a previous study [18] found no segregation of Al to grain boundaries in VCrMnFe + Al.

Figure 11 shows that there is enrichment of Al and Ga along the grain boundaries in regions near the boundary between sigma containing areas and areas that do not contain sigma phase. In the case of Ga, the data presented in figure 11 suggests the enrichment profile across the grain boundaries is substantial, especially with regards to its width (>5 μm). Relating the bulk Ga content to the matrix content would then be entirely dependent upon grain size. In a large grained sample, such as the one examined here, the difference should be negligible. In a small grained, on the order of 1 μm, the enrichment profiles from grain boundaries should overlap considerably, producing a more uniform concentration distribution. Only in intermediate sized grains would the result be an issue. Grain boundary segregation can therefore not be

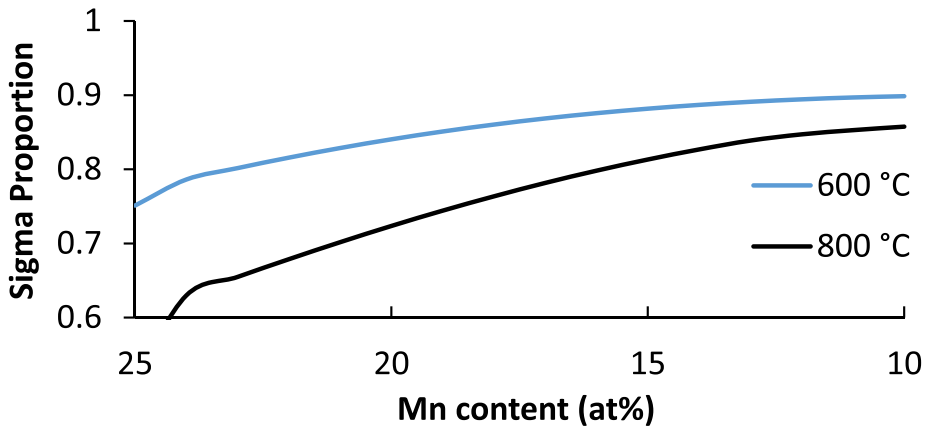

Figure 12. Proportion of Sigma phase in VCrMnFe at 600 and 800 °C, with the Mn content varied along the x axis. Calculated using Thermocalc's HEA4 database.

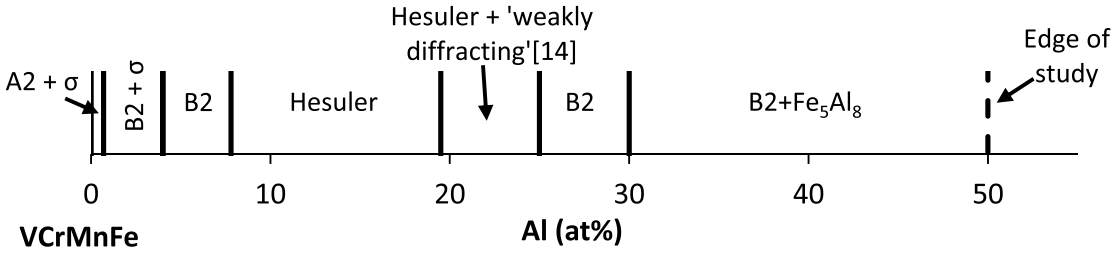

Figure 13. Partial empirical phase diagram of VCrMnFe–Al measured following heat treatment of 800 °C for 240 h followed by 600 °C for 240 h. The dotted line is not the end of the phase field, rather the end of the data presented in this paper.

considered a limitation exclusive to this diffusion couple study, it also applies to bulk alloys as they are typically not single grains.

In the VCrMnFe–Sn diffusion couple, the enrichment of Sn at the grain boundaries was very high (M_3Sn coated the boundaries), which induced a significant difference between the bulk and matrix Sn contents measured. The bulk concentration in the Sn-rich region (5.1 at% Sn) can be taken as an upper limit of bulk Sn content necessary to prevent sigma phase forming. The lower Sn content seen at the edge of the Sn-enriched region and the region containing sigma phase (2.0 at% Sn) may be taken as the necessary *matrix* Sn concentration for sigma phase suppression, which is not necessarily equal to the bulk concentration. It is also important to note that the Sn-enriched phase was not observed solely at the grain boundaries. It therefore cannot be stated that this phase was only observed due to excessive Sn enrichment at the grain boundaries.

Both table 2 and figure 4 show a clear reduction in Mn content in the Sn-enriched region. This type of depletion was only observed in the Sn sample. Some of the Mn reduction can be attributed to segregation to regions such as the M_3Sn phase, although not all of it. There are too many variables to pinpoint why this happened in only the Sn sample. However, it does make drawing conclusions about the effect of Sn on VCrMnFe more difficult as the ratio of these elements has been altered. Figure 12 shows the proportions of sigma phase within a $VCrMn_xFe$ alloy as predicted by Thermocalc (using the HEA4 database). It suggests that reducing the Mn content should increase the stability of sigma phase. This is reasonable given that the higher Mn content alloy VCrMn does not form sigma phase at the temperatures used to heat treat the alloys in this study [5]. Thus, it is reasonable to treat the Sn contents seen to prevent sigma phase formation in this study as upper rather than lower limits in the VCrMnFe alloy system.

4.2. VCrMnFe–Al phase diagram

The TEM foils analysed in the alloy with Al additions have enabled an expansion of the VCrMnFe–Al pseudo-binary phase diagram measured in [18]. This is shown in figure 13. With the exception of sigma phase, all the phases found across this wide phase space were cubic with lattice constants equal to a multiple of the BCC (A2) lattice constant, and coherent with each other.

4.3. Implications of findings

The investigation demonstrated that Ga and Sn are not suitable additions to VCrMnFe to create alloys for fusion applications. Their addition led to grain boundary embrittlement, and the addition of Ga also resulted in the formation of a hard secondary phase (M_3Ga) which is unlikely to prove beneficial to properties. However, the additional phases observed to form within these systems are still beneficial for the wider HEA field in terms of predicting future phase formation.

Al remains a promising addition, and this work has now identified more precisely the minimum level of Al required to suppress sigma phase formation. This is important because, as discussed in the introduction, the addition of high levels of Al has been found to lead to high levels of ordering, delivering high hardness and brittleness [18]. It is now known that future alloys may require only 4 at% Al to avoid sigma phase, increasing the chance that an alloy may be found that does not form sigma phase and does not excessively harden through ordering (and embrittle).

This work has demonstrated that diffusion couples are a useful tool for the design and investigation of multi-principal element alloys. However, care must be taken when assessing the results as preferential diffusion along grain boundaries (in the case of some elements) makes interpretation of results more complex.

5. Conclusions

- A diffusion couple experiment was successful in creating a concentration gradient in a low activation multi-principal element alloy at 800 °C. Three elements; Ga, Sn and Al were all successfully dissolved into VCrMnFe.
- The pseudo-binary VCrMnFe–Al phase diagram has been significantly extended and sharpened with respect to compositional boundaries, as measured after heat treatment of 800 °C for 240 h followed by 600 °C for 240 h.
- The range of Al compositions necessary to prevent sigma phase formation in the VCrMnFe system can be reduced from 2.3–6.6 at% found in the previous study [18] to 4.0 $\pm$ 0.5 at%.
- Similar matrix contents of Ga and Sn (3.0 $\pm$ 0.5 at% Ga and 2.0 $\pm$ 0.8 at% respectively) were found to also be sufficient to prevent sigma phase from forming in VCrMnFe, although these measurements were complicated by enrichments at the grain boundaries, making their matrix contents different from their bulk contents. Both these elements were responsible for causing grain boundary embrittlement, ruling themselves out for any practical applications.
- Both Sn and Ga were found to form M_3Sn and M_3Ga phases respectively. The M_3Sn phase formed at Sn concentrations lower than those necessary to prevent sigma phase formation.
- Additions of Sn and Ga embrittled the VCrMnFe, meaning they are unlikely to be suitable additions to VCrMnFe for creating structural alloys.
- $VCrMnFeAl_x$ alloys remain a promising avenue for exploration for future fusion applications.

Data availability statement

The data that support the findings of this study are openly available at the following URL/DOI: https://zenodo.org/record/7575474.

Acknowledgments

The authors wish to knowledge funding from the EPSRC under Grants EP/R021546/1 and EP/R021864/1. We also wish to acknowledge the support of the Henry Royce Institute for Advanced Materials for E J Pickering's time, as well as access to the FEI Talos electron microscope at Royce@Manchester, funded through EPSRC Grants EP/R00661X/1, EP/S019367/1, EP/P025021/1 and EP/P025498/1.

ORCID iDs

M Rigby https://orcid.org/0000-0002-3421-2541
E J Pickering https://orcid.org/0000-0002-7516-868X

References

[1] Pickering E J and Jones N G 2016 High-entropy alloys: a critical assessment of their founding principles and future prospects *Int. Mater. Rev.* **61** 183–202
[2] Moschetti M, Burr P, Obbard E, Kruzic J J, Hosemann P and Gludovatz B 2022 Design considerations for high entropy alloys in advanced nuclear applications *J. Nucl. Mater.* **567** 153814
[3] Gilbert M R, Fleming M and Sublet J-C 2017 Automated inventory and material science scoping calculations under fission and fusion conditions *Nucl. Eng. Technol.* **49** 1346–53
[4] Gilbert M R, Eade T, Rey T, Vale R, Bachmann C, Fischer U and Taylor N P 2019 Waste implications from minor impurities in European DEMO materials *Nucl. Fusion* **59** 076015
[5] Barron P J, Carruthers A W, Fellowes J W, Jones N G, Dawson H and Pickering E J 2020 Towards V-based high-entropy alloys for nuclear fusion applications *Scr. Mater.* **176** 12–16
[6] El-Atwani O *et al* 2018 Outstanding radiation resistance of tungsten-based high entropy alloys *Sci. Adv.* **5** 1–10
[7] Decker P, Naujoks D, Langenkämper D, Somsen C and Ludwig A 2017 High-throughput structural and functional characterization of the thin film materials system Ni-Co-Al *ACS Comb. Sci.* **19** 618–24
[8] Kusne A G *et al* 2020 On-the-fly closed-loop materials discovery via Bayesian active learning *Nat. Commun.* **11** 1–11
[9] Ludwig A 2019 Discovery of new materials using combinatorial synthesis and high-throughput characterization of thin-film materials libraries combined with computational methods *npj Comput. Mater.* **5** 70
[10] Melia M A, Whetten S R, Puckett R, Jones M, Heiden M J, Argibay N and Kustas A B 2020 High-throughput additive manufacturing and characterization of refractory high entropy alloys *Appl. Mater. Today* **19** 100560
[11] Moorehead M, Bertsch K, Niezgoda M, Parkin C, Elbakhshwan M, Sridharan K, Zhang C, Thoma D and Couet A 2020 High-throughput synthesis of Mo-Nb-Ta-W high-entropy alloys via additive manufacturing *Mater. Des.* **187** 108358
[12] Tabor D P *et al* 2018 Accelerating the discovery of materials for clean energy in the era of smart automation *Nat. Rev. Mater.* **3** 5–20
[13] Connor L D 2016 *et al Investigation of Superalloy Composition Using High Throughput Thin Film Synthesis and Synchrotron x-ray Diffraction* pp 45–54
[14] Keil T, Bruder E and Durst K 2019 Exploring the compositional parameter space of high-entropy alloys using a diffusion couple approach *Mater. Des.* **176** 107816
[15] Carruthers A W *et al* 2020 Novel reduced-activation TiVCrFe based high entropy alloys *J. Alloys Compd.* **856** 157399
[16] Pickering E J, Carruthers A W, Barron P J, Middleburgh S C, Armstrong D E J and Gandy A S 2021 High-entropy alloys for advanced nuclear applications *Entropy* **23** 1–28
[17] Hsieh C-C and Wu W 2012 Overview of intermetallic sigma (σ) phase precipitation in stainless steels *ISRN Metall.* **2012** 1–16
[18] Carruthers A W, Shahmir H, Hardwick L, Goodall R, Gandy A S and Pickering E J 2021 An assessment of the high-entropy alloy system VCrMnFeAlx *J. Alloys Compd.* **888** 161525
[19] Villars P and Okamoto H (eds) 2012 Mn-Sn-V isothermal section of ternary phase diagram: datasheet from 'PAULING FILE multinaries edition (Tokyo: Springer) (available at: https://materials.springer.com/isp/phase-diagram/docs/c_0201118)
[20] Villars P and Okamoto H (eds) 2012 Cr-Fe-Ga isothermal section of ternary phase diagram: datasheet from 'PAULING FILE multinaries edition (Tokyo: Springer) (available at: https://materials.springer.com/isp/phase-diagram/docs/c_2000114)
[21] Stevie F A *et al* 2001 Application of focused ion beam lift-out specimen preparation to TEM, SEM, STEM, AES and SIMS analysis *Surf. Interface Anal.* **31** 345–51
[22] Basile F, Lecocq P and Michel A 1969 Etude des composes V3Sn, Fe3Sn, de leurs solutions solides et de la phase Fe3.4-xVxSn0.6 *Ann. Chim.* **4** 297–308
[23] Singh U P, Pal A K, Chandrasekaran L and Gupta K P 1968 Study of the manganese-rich end of Mn-Sn sytem *Trans. Metall. Soc. AIME* **242** 1661–3
[24] Nachtrab W T and Chou Y T 1984 Grain boundary segregation of copper, tin and antimony in C-Mn steels at 900 °C *J. Mater. Sci.* **19** 2136–44
[25] Pereiro-López E, Ludwig W, Bellet D and Baruchel J 2003 Liquid-metal wetting at grain boundaries: a synchrotron-micro-radiographic investigation *Defect Diffus. Forum* **216–217** 241–8